

Real-Time Pollen Identification using Holographic Imaging and Fluorescence Measurements

Elias Graf^{1,*}, Sophie Erb^{2,3,*}, Yanick Zeder^{1,*}, Simone Lionetti⁴, Alexis Berne³, Bernard Clot², Gian Lieberherr², Fiona Tummon², Pascal Wullschleger⁴, Benoît Crouzy²

*These authors contributed equally to this work.

¹Swisens AG, Horw, CH-6048, Switzerland

²Federal Office of Meteorology and Climatology MeteoSwiss, Chemin de l'Aérologie, CH-1530, Payerne, Switzerland

³Environmental Remote Sensing Laboratory (LTE), École Polytechnique Fédérale de Lausanne, Lausanne, Switzerland

⁴Algorithmic Business Research Lab (ABIZ), Lucerne University of Applied Sciences and Arts, Lucerne, Switzerland

Correspondence to: Sophie Erb (sophie.erb@meteoswiss.ch)

Abstract. Over the past few years, a diverse range of automatic real-time instruments has been developed to respond to the needs of end users in terms of information about atmospheric bioaerosols. One of them, the SwisensPoleno Jupiter, is an airflow cytometer used for operational automatic bioaerosol monitoring. The instrument records holographic images and fluorescence information for single aerosol particles, which can be used for identification of several aerosol types, in particular different pollen taxa. To improve the pollen identification algorithm applied to the SwisensPoleno Jupiter and currently based only on the holography data, we explore the impact of merging fluorescence spectra measurements with holographic images. We demonstrate, using manually generated data, that combining information from these two sources results in a considerable improvement in the classification performance compared to using only a single source (balanced accuracy of 0.992 vs. 0.968 and 0.878). This increase in performance can be ascribed to the fact that often classes which are difficult to resolve using holography alone can be well identified using fluorescence and vice versa. We also present a detailed statistical analysis of the features of the pollen grains that are measured and provide a robust, physically-based insight into the algorithm's identification process. The results are expected to have a direct impact on operational pollen identification models, particularly improving the recognition of taxa responsible for respiratory allergies.

1. Introduction

Over the past decades a considerable increase in aeroallergen-related diseases such as asthma or allergic rhinitis has been observed (Ring et al. 2001; Woolcock et al. 2001; Woolcock et Peat 2007). This has resulted in a rise in associated direct and indirect health costs in terms of hospitalisation, medication costs and absence from work (Zuberbier et al. 2014; Greiner et al. 2011). Currently, the prevalence of pollen allergy ranges between 10 to 30% of the population in Westernised countries and up to 40% of children in high-income countries (Pawankar et al. 2011). In future, the relevance of pollen as an allergen may increase further as a result of climate change, which perturbs the life cycle of plants through drier environmental conditions and increased temperatures. Stressed plants tend to have an earlier and/or longer blooming season (Ziello et al. 2012) and

33 produce more pollen with higher concentrations of allergens (Damialis et al. 2019; Beggs 2016; D'Amato et al. 2016), possibly
34 further contributing to the increase and severity of allergic diseases. For these reasons, systems to measure airborne pollen
35 concentrations are essential to meet public health challenges associated with respiratory allergies. Through real-time
36 measurements and the development of forecast models (Chappuis et al. 2020), they can help reduce health costs with better
37 diagnosis and prevention, thus helping patients to better manage their symptoms.

38
39 Most European countries started monitoring pollen in the second half of the 20th century using Hirst-type instruments (Hirst
40 1952) with manual identification and counting part of the process (Clot 2003; Spieksma 1990). However, this method provides
41 data at low time resolution, typically daily mean values, after a processing time of up to 10 days. The spread of pollen grains
42 on the collection band and the limited sampling (Oteros et al. 2017) mean that data at higher temporal resolutions, or at low
43 concentrations (below 10 pollen grains/m³), have considerably increased uncertainty (Adamov et al. 2021). Although little
44 data is available to study atmospheric pollen phenomena at high temporal resolutions, it is widely expected that pollen
45 production and dispersal processes take place at sub-daily scales since they are highly influenced by local meteorological
46 environmental conditions (Rojo et al. 2015; Rantio-Lehtimäki 1994). Provision of real-time pollen data is also crucial for
47 forecasting purposes, since models can then integrate these real-time data to deliver considerably improved forecasts (Sofiev
48 2019).

49
50 Over the past few years, several instruments designed for real-time pollen monitoring have come onto the market (Crouzy et
51 al. 2016; Oteros et al. 2015), as comprehensively reviewed in previous work (Huffman et al. 2020; Buters et al. 2022; Maya-
52 Manzano et al. 2023). Among the most promising instruments are airflow cytometers which allow the characterisation of
53 particles almost in real-time as they pass through the instrument and enable continuous monitoring with high temporal
54 resolution (10 minutes as for weather parameters or below) over a whole season. In particular, the SwisensPoleno Jupiter
55 (developed by Swisens AG, Switzerland) is an instrument for bioaerosol identification which can take in-flight holographic
56 images of particles and measure their fluorescence (FL hereafter) (Sauvageat et al. 2020; Tummon et al. 2021; Lieberherr et
57 al. 2021). Coupled with a machine learning (ML) algorithm, it has been shown to perform well for pollen monitoring even if
58 the algorithm uses just the holographic data (Sauvageat et al. 2020; Crouzy et al. 2022; Maya-Manzano et al. 2023).

59
60 The FL data has to date not been used for pollen identification with the SwisensPoleno Jupiter. Sauvageat et al. 2020 reached
61 an accuracy above 96% for eight of the main allergenic pollen species in central Europe (*Ambrosia artemisiifolia*, *Corylus*
62 *avellana*, *Dactylis glomerata*, *Fagus sylvatica*, *Fraxinus excelsior*, *Pinus sylvestris*, *Quercus robur* and *Urtica dioica*) using
63 only holographic images. However, some species have similar morphologies which can cause misclassifications and thus lower
64 the algorithm performance, as previously identified in Sauvageat et al. 2020. In this paper, we investigate whether FL helps
65 discriminate single pollen grains between different allergenic taxa based on their chemical compositions to reduce the level of

66 confusion resulting from their similar shapes. Moreover, we also verify whether the FL measurements are consistent for each
67 species when using different SwisensPoleno units.

68 **2. Material and Methods**

69 In this work we investigate the impact of including the set of FL measurements, constituting the particle FL spectra, as input
70 for pollen identification using artificial neural networks. We trained and assessed the performance of three neural networks
71 with the same dataset but using different inputs: only holographic images (holo), only FL spectra (FL), or both (combined).
72 The performance of each model is evaluated using classical metrics, here the balanced accuracy, the F1-score, and Matthew's
73 Correlation Coefficient (MCC) as defined in Chicco et al. 2020, as well as the (relative) error rate derived from the accuracy.

74 **2.1. Pollen holography and fluorescence dataset**

75 The SwisensPoleno Jupiter measures particles in flight, in the size range from 0.5 to 300 μm , as they pass through the
76 instrument. When a particle triggers the detector, holographic images are taken by two cameras which are both orthogonal to
77 the direction of flight and at 90° to each other. These images are greyscale with a resolution of 200 by 200 pixels after numerical
78 reconstruction and cropping, with each pixel representing a square of $0.595 \times 0.595 \mu\text{m}$ in the physical domain. Right after the
79 holographic images, FL is measured using the Laser Induced Fluorescence (LIF) method. FL is then sequentially induced by
80 three excitation sources and captured in five different wavelength channels, for a total of 15 measured FL intensities. For each
81 source, the FL is induced by shooting at the particle at the moment it passes the detector and the FL subsequently emitted by
82 the particle is captured by Silicon Photomultipliers (SiPM). The FL lifetime is also measured but is not used in the present
83 work. The three different excitation wavelengths are 405, 365, and 280 nm, while the reception wavebands are 333-381, 411-
84 459, 465-501, 539-585, and 658-694 nm. In the following, we will refer to each waveband by its central wavelength, i.e., 357,
85 435, 483, 562, and 676 nm. Note that the first measurement channel is saturated by scattered light when the 365 nm excitation
86 source is activated. Also, for single-photon excitation, we expect to measure no signal in the first measurement channel when
87 the 405 nm source is active. This effectively reduces the useful intensity measurements to 13. The FL data requires additional
88 pre-processing to simplify its usability and improve robustness. More details on these steps are provided in Section 2.2. Finally,
89 the SwisensPoleno Jupiter also performs polarised scattered light measurements, which are however not used in the present
90 work. We therefore limit the analysis to characterisation of particle morphology using digital holography and chemical
91 composition with FL intensity measurements. From hereon, we refer to the set of holographic images and FL measurements
92 for each individual particle as "an event". A more extensive description of the data collection process is provided in Sauvageat
93 et al. 2020.

94
95 This study is based on a pollen dataset created by aerosolising freshly collected pollen at the Swiss Federal Office of
96 Meteorology and Climatology MeteoSwiss (hereafter MeteoSwiss) station in Payerne, Switzerland. In total, the dataset
97 consists of measurements from 57'300 pollen grains distributed among seven different wind-pollinated and allergy relevant

98 plant taxa as reported in Table 1. For simplicity, we will refer to these taxa also as "classes" and only the genus name will be
 99 used to refer to each of them. In Figure 1, we present examples of reconstructed images for the different classes considered in
 100 this work. To compare results across different instruments (of the same type), all measurements were performed using two
 101 SwisensPoleno Jupiter systems denoted P4 and P5. The counts for each pollen taxa and SwisensPoleno are also given in Table
 102 1.

103
 104 The pollen samples were collected from a single tree for *Alnus*, *Betula*, *Corylus*, *Fagus*, and *Quercus*, from two different trees
 105 for *Fraxinus*, and from a few neighbouring stems for the grass *Cynosurus*. After collection, pollen was brought to the outdoor
 106 measurement site and aerosolised. This was achieved using a SwisensAtomizer which disperses particles using a vibrating
 107 membrane and an airstream. Samples are thus scattered in a chamber and drawn into the instrument, producing a regular flow
 108 of pollen grains. To prevent the pollen from drying out, plants that were not more than 15 km away from the MeteoSwiss
 109 station were selected, which means it was possible to aerosolise samples soon after collection (usually within one hour). Pollen
 110 samples were analysed using two instruments one after another implying a time lag between the data for P4 and P5, which
 111 ranges from just 35 minutes for *Alnus* to 80 minutes for *Quercus* (the mean time lag is 60 minutes). For *Fraxinus* there is no
 112 such lag since the data come from two different samples that were measured on different days. Datasets for all the considered
 113 pollen taxa were created in 2020, except *Alnus* and *Corylus* which are from early 2021.

114

Class (common name)	Latin scientific name	Number of events for P4	Number of events for P5
Alder	<i>Alnus glutinosa</i>	8416	2643
Birch	<i>Betula pendula</i>	6128	5458
Hazel	<i>Corylus avellana</i>	4714	4444
Crested Dog's-Tail (Grass)	<i>Cynosurus cristatus</i>	5895	2117
Beech	<i>Fagus sylvatica</i>	2178	2827
Ash	<i>Fraxinus excelsior</i>	2557	4837
Oak	<i>Quercus robur</i>	3036	2050
	TOTAL	32924	24376

115 **Table 1: Distribution of pollen counts per taxa and Poleno.**

116

117 2.2. Data pre-processing

118 The datasets required to train the algorithms were generated as follows. First, the holographic data for each class were cleaned
 119 to eliminate any non-pollen events or events associated with other pollen taxa. This was achieved with additional filters on
 120 shape properties (image features computed after binarisation as described in Sauvageat et al. 2020), which were appropriately
 121 selected for every class by heuristic visual inspection of the holographic images. Thereafter, for each event the background

122 signal caused by scattered light was subtracted from the raw FL measurement. This background especially disturbs the low FL
123 intensity measurements where the scattered light dominates relative to the particle signal. The background signal was obtained
124 by conducting measurements with no particles present in the measurement chamber, leaving just the scattered light induced
125 by the excitation source. If the subtraction caused the final signal to be negative due to noise, the resulting value was set to
126 zero to avoid numerical instabilities that our ML model would not be able to deal with. Finally, since the absolute FL
127 compensated by the scattered light is still dependent on the measuring system, the particle size, and the particle position within
128 the measurement volume, we transformed it into relative FL. Namely, the relative fluorescence intensity r_{ij} for measurement
129 channel i and excitation source j is obtained by dividing the absolute FL intensity a_{ij} by the sum of the FL intensities on all
130 channels k for the same excitation source j :

$$131 \quad r_{ij} = \frac{a_{ij}}{\sum_k a_{kj}}$$

132 Using relative FL, although we lose the absolute FL intensities, allows measurement systems to be compared without specific
133 data modification. The inter-compatibility aspect is especially important when considering a measurement network. Thanks to
134 this standardisation, the same algorithm can be used for all systems in the network rather than adjusting the classification
135 algorithm individually for each measurement system.

136 **2.3. Data exploration**

137 Before applying any ML algorithm, it is important to explore the data to better understand their characteristics. In the following,
138 the distributions of the various holographic image features as well as typical relative FL spectra for the different pollen types
139 are investigated. We also explore the structure of the data using dimension reduction.

140
141 To get other characteristic features from the reconstructed holographic images, further image processing steps are conducted
142 using the Python package "Scikit" (Van der Walt et al. 2014). Physically-based particle features, such as the minor and major
143 axes, the area, the eccentricity, and the particle brightness (mean intensity of the pixels reproducing the particle) are computed
144 for each image separately. Other statistics were calculated based on image features, e.g., the equivalent area diameter defined
145 as the diameter of a circle with the same area as the particle. The distribution of these features for each pollen class and each
146 measurement system were analysed separately and are presented in the Results section.

147
148 As previously discussed, alongside the holography images, relative FL spectra are used for enhanced characterisation of the
149 pollen grains. During data exploration, we observed inconsistent results for the 405 nm laser excitation, which upon further
150 inspection revealed a misalignment of this laser in one of the measurement systems. For this reason, we will only use the 280
151 nm and 365 nm excitation throughout the rest of the present work. The distributions of the valid FL spectra are presented and
152 discussed in the Results section.

153

154 As a way to explore all the features of the dataset at once, we performed dimensionality reduction. We used the Uniform
155 Manifold Approximation and Projection (McInnes et al. 2018), called UMAP, on the input data of each model (holo, FL and
156 combined). This technique allows us to plot multidimensional data as points on a plane, therefore it gives an insight on how
157 similar/different data points are depending on how far from another they are in the plane.

158 **2.4. Machine Learning Model**

159 To handle the classification task, we randomly split the data into training (75%) and test (25%) sets and chose a multi-layer
160 "deep" artificial neural network to learn how to identify pollen grains based on the training set. This network maps input data
161 from the holographic images and relative FL spectra to the different pollen classes. The full network, built using the ML
162 framework Keras (Chollet et al. 2015), is shown in Figure 2. To handle the image input, an EfficientNet B0 model pre-trained
163 on ImageNet is used (Tan et Le 2019). It achieves state-of-the-art performance for classification tasks. For treating the spectral
164 information, a single fully connected (denoted FC hereafter) hidden layer with 255 neurons is used. As a pre-trained model,
165 the parameters of EfficientNet B0 are frozen and therefore not modified in the training on the pollen dataset. However, the
166 parameters of the layers after it are optimised according to the training data. The results of the two feature extraction networks
167 are concatenated, then dropout is added and finally the result is passed to the decision layer. The width of this FC decision
168 layer matches the number of classes (seven in this case). Lastly, the output is normalised by a softmax layer to obtain a
169 probability distribution. To compute the loss, we used the cross-entropy function between the predicted and reference classes.
170 To ensure a fair comparison, each model was trained for exactly 200 epochs. In training runs where only images or only relative
171 FL spectra were used, the path not used was removed from the model graph (Figure 2). The figure shows the model with both
172 features active.

173 The models were evaluated using a test set consisting of 25% of the data from both instruments, sampled randomly. We used
174 balanced accuracy, F1 score and Matthew's Correlation Coefficient (MCC) as metrics to assess the model performance. For
175 accuracy, the corresponding confidence intervals were calculated via normal approximation as explained in Raschka 2020. It
176 is important to note that the model used here is a baseline and has not undergone hyper-parameter optimisation, therefore no
177 validation set has been defined in order to keep a maximum of data for training. This means that a degradation of scores is
178 possible when applying the model to operational data as all sorts of pollen taxa can be encountered considering that other
179 particles are filtered out before the classification. Nonetheless, the present study does not aim to provide an operational model
180 but simply investigate the potential of using FL as a complement to holography for single particle identification.

181 **3. Results**

182 **3.1. Feature observations**

183 Important observations can already be made by looking at basic geometrical features derived from holographic images. As an
184 example, we consider the distributions of equivalent area diameter and eccentricity in Figure 3 (a) and (b). Note that for

185 geometrical features, the value associated with each particle is the largest result obtained for the pair of holographic images.
186 Regarding the equivalent area diameter, its distribution provides information about the size of the pollen grains for a given
187 class. As illustrated in Figure 3 (a), *Fagus* pollen grains are typically large with a maximum equivalent area diameter of 45-55
188 μm , which corresponds to the literature (Halbritter et al. 2021) and is clearly larger than all other classes we considered in our
189 study. Conversely, the distribution of the eccentricity gives an insight on how round the pollen grains are. In that case,
190 *Cynosurus* pollen grains have the roundest shape with a maximal eccentricity between 0.4 and 0.55 (0 representing a circle
191 and 1 an ellipse), whereas *Quercus*' values are in the range 0.8-0.9 due to its more elliptical shape. These characteristics can
192 also be observed on the holographic images in Figure 1. While the eccentricity is used to give a hint on the symmetry of the
193 pollen grain, further metrics could be introduced to further quantify symmetry. This was not implemented in the present study
194 as feature extraction is done automatically by the convolutional neural network.

196 The distributions of the relative FL spectra allow us to identify some classes that have distinct FL signatures. Figure 3 (c) and
197 (d) show the distribution of the relative FL for the two excitation-emission combinations where the differences between taxa
198 are the largest. The excitation sources are at 280 and 365 nm with emission channels at 357 and 435 nm respectively. In Figure
199 3, we observe, for both plot (c) and (d), clear differences in relative FL for *Cynosurus*, which presents considerably higher
200 values compared to the other taxa. In addition, differences between instruments show that P4 and P5 have similar
201 measurements in the 280/357 nm but P5 has significantly lower measurements for *Corylus* and *Cynosurus* in the 365/435 nm.
202 Overall, all combinations of excitation sources and emission channels provide relevant information for pollen characterisation
203 and the ones presented in Figure 3 (c) and (d) represent well the type of patterns that can be observed.

205 Finally, the UMAP plots, given in the left column of Figure 4, show how different or similar are the image and FL features of
206 each taxon. We observe a clear distinction based on morphology (Figure 4 (a)) for *Fagus* and *Quercus*, with *Cynosurus* also
207 having only little overlap with *Corylus*. However, the latter and especially *Betula* and *Alnus* are clearly mixed up. In Figure 4
208 (b), the UMAP on FL spectra does not exhibit the same group structure as for morphology. Here, *Fagus* and *Cynosurus* are
209 plainly detached from the remaining groups which are themselves imbricated. Ultimately, all groups are fully separated when
210 building the UMAP on both morphology and FL features. We observe a correspondence between the separation of groups on
211 the UMAPs and the capacity of the ML model to classify those classes correctly.

212 3.2. Classification performance

213 The classification results for each model are given as confusion matrices in Figure 4 and summarised in Table 2. We observe
214 in these results that the holo model globally performs better than the FL model when training on a single modality. The FL
215 model indeed encounters difficulties distinguishing some classes such as *Quercus* and *Fraxinus* or *Betula* and *Corylus* (Figure
216 4 (b)) which exhibit similar relative FL spectra. When considering the morphology of *Quercus* and *Fraxinus* (Figure 3 (a) and
217 (b)), it is not surprising that the holography model performs better at differentiating these classes as they present significantly

218 distinct shapes. As the performance for the single-input models here is already (very) high, minor dips in performance can
 219 make a notable difference. Combining holography and FL improves the performance compared to the single input models for
 220 every taxon considered, except for *Fagus* and *Cynosurus* that already obtain perfect scores with single input models. The
 221 performance gain is noteworthy as the combined model achieves an overall balanced accuracy of 99.2% compared to either
 222 96.8% or 87.8% for the individual holography or FL models respectively. As a complement, the confidence intervals associated
 223 with the accuracy of each model for each taxon are displayed in Figure 5. The non-overlapping of the confidence intervals
 224 indicates a statistical difference between accuracies. The combined model outperforms both single-input models for five of the
 225 seven taxa, namely, *Alnus*, *Betula*, *Corylus*, *Fraxinus* and *Quercus*. Thus, logically, the balanced accuracies of the holo and
 226 FL models are significantly lower than that of the combined model (see Table 2). It follows that the absolute error rates, defined
 227 as 1 minus the accuracy, of the holo- (3.2%) and FL-only (12.2%) models are respectively 4 and 15 times higher than that of
 228 the combined model (0.8%). This indicates that mistakes in particle identification occur for roughly 3 particles over 100 for
 229 the holo model, 12 particles over 100 for the FL model but less than 1 particle over 100 for the combined model.

230

Model	Balanced accuracy	F1-score	MCC
Holography only	0.968, [0.965; 0.970]	0.964	0.958
FL only	0.878, [0.874; 0.882]	0.890	0.874
Combined	0.992, [0.991; 0.993]	0.992	0.991

231 **Table 2: Classification performance of each model. The balanced accuracy, with its associated 95% confidence interval,**
 232 **represents the average of the recalls (ratio of correct prediction over total count for each class), ranging from 0 to 1.**
 233 **The F1-score is the harmonic mean of the precision and recall, ranging from 0 to 1 and MCC stands for Matthew's**
 234 **Correlation Coefficient and is a robust metric for classification performance, ranging from -1 to 1.**

235 4. Discussion

236 The results based on manually generated data show that combining FL with holography leads to a substantial identification
 237 performance gain. The differences between the combined model accuracy and both single-input models confirm the findings
 238 from the UMAPs. This demonstrates that by combining the two inputs, the complementary morphological and biochemical
 239 properties of pollen grains can be used for a better classification. Although it seems small, the gain in accuracy is important
 240 for the field of aerobiology and specifically pollen monitoring since pollen grains only represent a minor part of all the particles
 241 in the air. Since pollen concentrations typically range from a few grains (< 10) to a few hundred grains per cubic metre, and
 242 the thresholds for allergy symptoms are usually around a few tens of grains per cubic metre (Gehrig Bichsel et al. 2017;
 243 Pollen.lu 2003), misclassifications can have an impact on the information provided to allergic people. Above all, high
 244 identification accuracy is particularly important for plants with highly allergenic pollen such as *Ambrosia artemisiifolia*
 245 (common ragweed) as a few grains are sufficient to cause allergy symptoms.

246

247 Not only is the combined model's accuracy superior to the other models, but this gain is specifically important for some key
248 pollen taxa. Indeed, the group of *Alnus*, *Betula* and *Corylus*, all from the Betulaceae family, is known to be difficult to classify
249 accurately and presents a very high allergic potency with possible cross-reactivity in central and northern Europe (Puc et
250 Kasprzyk 2013). Thus, the excellent classification performance obtained here opens the gate towards better monitoring by
251 using holography together with fluorescence data. In addition, the consistent FL signal in between instruments and the available
252 excitation sources and measurement channels characterise single pollen grains precisely even though the 405 nm excitation
253 source was set aside. Also, the combinations of excitation and emission wavelengths used in the Poleno correspond to the most
254 prominent fluorescence modes for a variety of dry pollen studied in (Pöhlker et al. 2013). The coherence between our results
255 and those from Pöhlker et al. 2013 brings confidence into our measurements and the stability of the Poleno. In future work,
256 the 405 nm excitation source needs to be included to verify its potential for improvement.

257

258 When working with images, choosing neural networks for classification is the obvious solution to be sure not to lose
259 information by using the image itself as input. However, the discrimination of pollen taxa using the UMAP dimension
260 reduction method shows that working with features derived from the holographic images is also a possibility for pollen
261 classification. Future work testing other machine learning methods on image features and fluorescence spectra needs to be
262 conducted as other classifiers may perform similarly while being cheaper in terms of computational resources. In addition, the
263 main limitation of this study, focusing on a reduced number of pollen taxa and manually generated data, should be overcome
264 in following work by gathering more data to train a broader model and test it on operational data.

265

266 In the end, we expect the benefit of combining holography with FL measurements for pollen classification to have a positive
267 impact on the capacity of models to discriminate different pollen taxa. Moreover, in an operational setup, the benefit of using
268 FL in addition to holography could be even higher as it would allow for an easy distinction between biological and non-
269 biological particles (e.g. water droplets, sand particles or dust) assuming that they do not fluoresce. Yet, the extent of the gain
270 in the real case scenario remains to be quantified as the dataset used in this study probably does not catch all the environmental
271 variability. For example, in ambient air, pollen can break into fragments also impacting allergy sufferers but not currently
272 monitored.

273 5. Conclusion

274 The present study demonstrates the potential of using FL measurements as a complementary input to holographic images for
275 single-grain pollen identification using the SwisensPoleno and ML algorithms for the most important allergy causing pollen
276 taxa in Central Europe. The capacity of the ML model to identify pollen grains depends on both inputs and they compensate
277 each other when one does not provide enough information for accurate identification. As a result, the performance of the
278 combined model is systematically higher than either of the models trained with a single input. The restricted and manually

279 created dataset used in this study has several limitations, but it still provides strong evidence for the complementary role of FL
280 and holography.

281

282 In conclusion, we recommend the use of relative FL as a secondary input for automatic pollen identification using the
283 SwisensPoleno Jupiter. In this study, we tested its contribution on a restricted dataset, showing that the contribution of FL is
284 of great value for operational networks where similar pollen taxa can be encountered. Finally, the use of relative FL for
285 automatic pollen identification further opens the door towards a larger and more precise monitoring of bioaerosols. For
286 example, objects which are challenging to identify using holographic imaging only, such as fungal spores, could be added to
287 the panel of particles.

288

289 **Author contribution**

290 EG, SE and YZ conducted the study and contributed equally as main authors. SL guided the machine learning aspects and
291 supervised PW in his work on the relative fluorescence. AB, BCl, GL and FT contributed to writing, and BC_r supervised the
292 study and contributed to writing.

293

294 **Competing interests**

295 EG and YZ are employees of Swisens AG, and AB is a member of the editorial board of AMT. The investigations were carried
296 out in compliance with good scientific practices and the declared relationships have no effect on the results presented. The
297 peer-review process was guided by an independent editor, and the authors have also no other competing interests to declare.

298

299 **Acknowledgements**

300 We would like to thank all the co-authors for their support, advice and help in the various aspects of this study. This work was
301 partly funded by the Swiss National Science Foundation (IZCOZO_198117) and by Swisens (AG).

302 **References**

- 303 Adamov, S., Lemonis, N., Clot, B., Crouzy, B., Gehrig, R., Graber, M. J., ... & Tummon, F. (2021). On the measurement
304 uncertainty of Hirst-type volumetric pollen and spore samplers. *Aerobiologia*, 1-15.
- 305 Beggs, Paul J., ed. (2016). Half-title-page. In *Impacts of Climate Change on Allergens and Allergic Diseases*, i-ii. Cambridge:
306 Cambridge University Press.
- 307 Buters, J., Clot, B., Galán, C. et al. Automatic detection of airborne pollen: an overview. *Aerobiologia* (2022).
308 <https://doi.org/10.1007/s10453-022-09750-x>
- 309 Chappuis, C., Tummon, F., Clot, B., Konzelmann, T., Calpini, B., & Crouzy, B. (2020). Automatic pollen monitoring: first
310 insights from hourly data. *Aerobiologia*, 36(2), 159-170.
- 311 Chollet, F., & others. (2015). Keras. GitHub. Retrieved from <https://github.com/fchollet/keras>
- 312 Chicco, D., Jurman, G. The advantages of the Matthews correlation coefficient (MCC) over F1 score and accuracy in binary
313 classification evaluation. *BMC Genomics* 21, 6 (2020). <https://doi.org/10.1186/s12864-019-6413-7>
- 314 Clot, Bernard. (2003). « Trends in Airborne Pollen: An Overview of 21 Years of Data in Neuchâtel (Switzerland) ». *Aerobiologia* 19 (3): 227-34. <https://doi.org/10.1023/B:AERO.0000006572.53105.17>.
- 315
- 316 Crouzy, Benoît, Michelle Stella, Thomas Konzelmann, Bertrand Calpini, et Bernard Clot. (2016). « All-optical automatic
317 pollen identification: Towards an operational system ». *Atmospheric Environment* 140: 202-212.
318 <https://doi.org/10.1016/j.atmosenv.2016.05.062>.
- 319 Crouzy, B., Lieberherr, G., Tummon, F. et al. False positives: handling them operationally for automatic pollen monitoring.
320 *Aerobiologia* 38, 429–432 (2022). <https://doi.org/10.1007/s10453-022-09757-4>
- 321 D’Amato, Gennaro, Ruby Pawankar, Carolina Vitale, Maurizia Lanza, Antonio Molino, Anna Stanziola, Alessandro Sanduzzi,
322 Alessandro Vatrella, et Maria D’Amato. (2016). « Climate Change and Air Pollution: Effects on Respiratory Allergy ». *Allergy, Asthma & Immunology Research* 8 (5): 391-95. <https://doi.org/10.4168/aaair.2016.8.5.391>.
- 323
- 324 Damialis, Athanasios, Claudia Traidl-Hoffmann, et Regina Treudler. (2019). « Climate Change and Pollen Allergies ». In
325 *Biodiversity and Health in the Face of Climate Change*, edited by Melissa R. Marselle, Jutta Stadler, Horst Korn,

326 Katherine N. Irvine, and Aletta Bonn, 47-66. Cham: Springer International Publishing. <https://doi.org/10.1007/978-3->
327 030-02318-8_3.

328 Gehrig Bichsel, Regula, Felix Maurer, et Cornelia Schwierz. (2017). « Regionale Pollenkalender der Schweiz - MétéoSuisse ».
329 Fachbericht Nr. 264. [https://www.meteosuisse.admin.ch/services-et-publications/publications/rapports-et-](https://www.meteosuisse.admin.ch/services-et-publications/publications/rapports-et-bulletins/2017/regionale-pollenkalender-der-schweiz.html)
330 [bulletins/2017/regionale-pollenkalender-der-schweiz.html](https://www.meteosuisse.admin.ch/services-et-publications/publications/rapports-et-bulletins/2017/regionale-pollenkalender-der-schweiz.html).

331 Greiner, Alexander N., Peter W. Hellings, Guiseppina Rotiroti, et Glenis K. Scadding. (2011). « Allergic Rhinitis ». *The Lancet*
332 378 (9809): 2112-22. [https://doi.org/10.1016/S0140-6736\(11\)60130-X](https://doi.org/10.1016/S0140-6736(11)60130-X).

333 Halbritter H., Bouchal J., Heigl H. 2021. *Fagus sylvatica*. In: PalDat - A palynological database.
334 https://www.palдат.org/pub/Fagus_sylvatica/304830;jsessionid=05C006636E5F5ED57525EEC2BFCC162F; accessed
335 2023-04-22

336 Hirst, J. M. (1952). « An Automatic Volumetric Spore Trap ». *Annals of Applied Biology* 39 (2): 257-65.
337 <https://doi.org/10.1111/j.1744-7348.1952.tb00904.x>.

338 Huffman, J. Alex, Anne E. Perring, Nicole J. Savage, Bernard Clot, Benoît Crouzy, Fiona Tummon, Ofir Shoshanim, et al.
339 (2020). « Real-time sensing of bioaerosols: Review and current perspectives ». *Aerosol Science and Technology* 54 (5):
340 465-95. <https://doi.org/10.1080/02786826.2019.1664724>.

341 « Impacts of Climate Change on Allergens and Allergic Diseases ». (2016). Cambridge Core. août 2016.
342 <https://doi.org/10.1017/CBO9781107272859>.

343 Lieberherr, Gian, Kevin Auderset, Bertrand Calpini, Bernard Clot, Benoît Crouzy, Martin Gysel-Beer, Thomas Konzelmann,
344 et al. (2021). « Assessment of Real-Time Bioaerosol Particle Counters Using Reference Chamber Experiments ».
345 *Atmospheric Measurement Techniques* 14 (12): 7693-7706. <https://doi.org/10.5194/amt-14-7693-2021>.

346 Maya-Manzano, J. M., Tummon, F., Abt, R., Allan, N., Bunderson, L., Clot, B., ... & Buters, J. (2023). Towards European
347 automatic bioaerosol monitoring: comparison of 9 automatic pollen observational instruments with classic Hirst-type
348 traps. *Science of the Total Environment*, 866, 161220.

349 McInnes, L., Healy, J., & Melville, J. (2018). Umap: Uniform manifold approximation and projection for dimension reduction.
350 arXiv preprint arXiv:1802.03426.

351 Oteros, Jose, Jeroen Buters, Gottfried Laven, Stefani Röseler, Reinhard Wachter, Carsten Schmidt-Weber, et Frieder Hofmann.
352 (2017). « Errors in Determining the Flow Rate of Hirst-Type Pollen Traps ». *Aerobiologia* 33 (2): 201-10.
353 <https://doi.org/10.1007/s10453-016-9467-x>.

354 Oteros, Jose, Gudrun Pusch, Ingrid Weichenmeier, Ulrich Heimann, Rouven Möller, Stefani Röseler, Claudia Traidl-
355 Hoffmann, Carsten Schmidt-Weber, et Jeroen T. M. Buters. (2015). « Automatic and Online Pollen Monitoring ». *International Archives of Allergy and Immunology* 167 (3): 158-66. <https://doi.org/10.1159/000436968>.

357 Pawankar, Ruby, G Canonica, ST Holgate, RF Lockey, et M Blaiss. (2011). « World Allergy Organisation (WAO) white book
358 on allergy ». *Wisconsin: World Allergy Organisation*.

359 Pöhlker, Christopher, J Alex Huffman, J-D Förster, et Ulrich Pöschl. (2013). « Autofluorescence of atmospheric bioaerosols:
360 spectral fingerprints and taxonomic trends of pollen ». *Atmospheric Measurement Techniques* 6 (12): 3369-92.

361 Pollen.lu, Ministère de la Santé, CHL. (2003). « Seuils critiques - Pollens ». 2003.
362 <http://www.pollen.lu/?qsPage=allergysteps&qsLanguage=Fra>.

363 Puc, Małgorzata, et Idalia Kasprzyk. (2013). « The patterns of Corylus and Alnus pollen seasons and pollination periods in
364 two Polish cities located in different climatic regions ». *Aerobiologia* 29 (4): 495-511.

365 Rantio-Lehtimäki, Auli. (1994). « Short, Medium and Long Range Transported Airborne Particles in Viability and
366 Antigenicity Analyses ». *Aerobiologia* 10 (2): 175. <https://doi.org/10.1007/BF02459233>.

367 Raschka, Sebastian. (2020). « Model Evaluation, Model Selection, and Algorithm Selection in Machine Learning ». arXiv.
368 <https://doi.org/10.48550/arXiv.1811.12808>.

369 Ring, Johannes, Ursula Krämer, Torsten Schäfer, et Heidrun Behrendt. (2001). « Why are allergies increasing? » *Current*
370 *Opinion in Immunology* 13 (6): 701-8. [https://doi.org/10.1016/S0952-7915\(01\)00282-5](https://doi.org/10.1016/S0952-7915(01)00282-5).

371 Rojo, Jesús, Patricia Salido, et Rosa Pérez-Badia. (2015). « Flower and Pollen Production in the ‘Cornicabra’ Olive (*Olea*
372 *Europaea* L.) Cultivar and the Influence of Environmental Factors ». *Trees* 29 (4): 1235-45.
373 <https://doi.org/10.1007/s00468-015-1203-6>.

374 Sauvageat, Eric, Yanick Zeder, Kevin Auderset, Bertrand Calpini, Bernard Clot, Benoît Crouzy, Thomas Konzelmann, Gian
375 Lieberherr, Fiona Tummon, et Konstantina Vasilatou. (2020). « Real-Time Pollen Monitoring Using Digital
376 Holography ». *Atmospheric Measurement Techniques* 13 (3): 1539-50. <https://doi.org/10.5194/amt-13-1539-2020>.

377 Sofiev, Mikhail. 2019. « On possibilities of assimilation of near-real-time pollen data by atmospheric composition models ». *Aerobiologia* 35 (3): 523-31.

378

379 Spieksma, Frits Th. M. (1990). « Pollinosis in Europe: New observations and developments ». *Review of Palaeobotany and*
380 *Palynology*, The Proceedings of the 7th International Palynological Congress (Part I), 64 (1): 35-40.
381 [https://doi.org/10.1016/0034-6667\(90\)90114-X](https://doi.org/10.1016/0034-6667(90)90114-X).

382 Tan, Mingxing, et Quoc Le. (2019). « Efficientnet: Rethinking model scaling for convolutional neural networks ». In
383 *International conference on machine learning*, 6105-14. PMLR.

384 Tummon, Fiona, Simon Adamov, Bernard Clot, Benoît Crouzy, Martin Gysel-Beer, Shigeto Kawashima, Gian Lieberherr, et
385 al. (2021). « A First Evaluation of Multiple Automatic Pollen Monitors Run in Parallel ». *Aerobiologia*, october.
386 <https://doi.org/10.1007/s10453-021-09729-0>.

387 Van der Walt, Stefan, Johannes L Schönberger, Juan Nunez-Iglesias, François Boulogne, Joshua D Warner, Neil Yager,
388 Emmanuelle Gouillart, et Tony Yu. (2014). « scikit-image: image processing in Python ». *PeerJ* 2: e453.

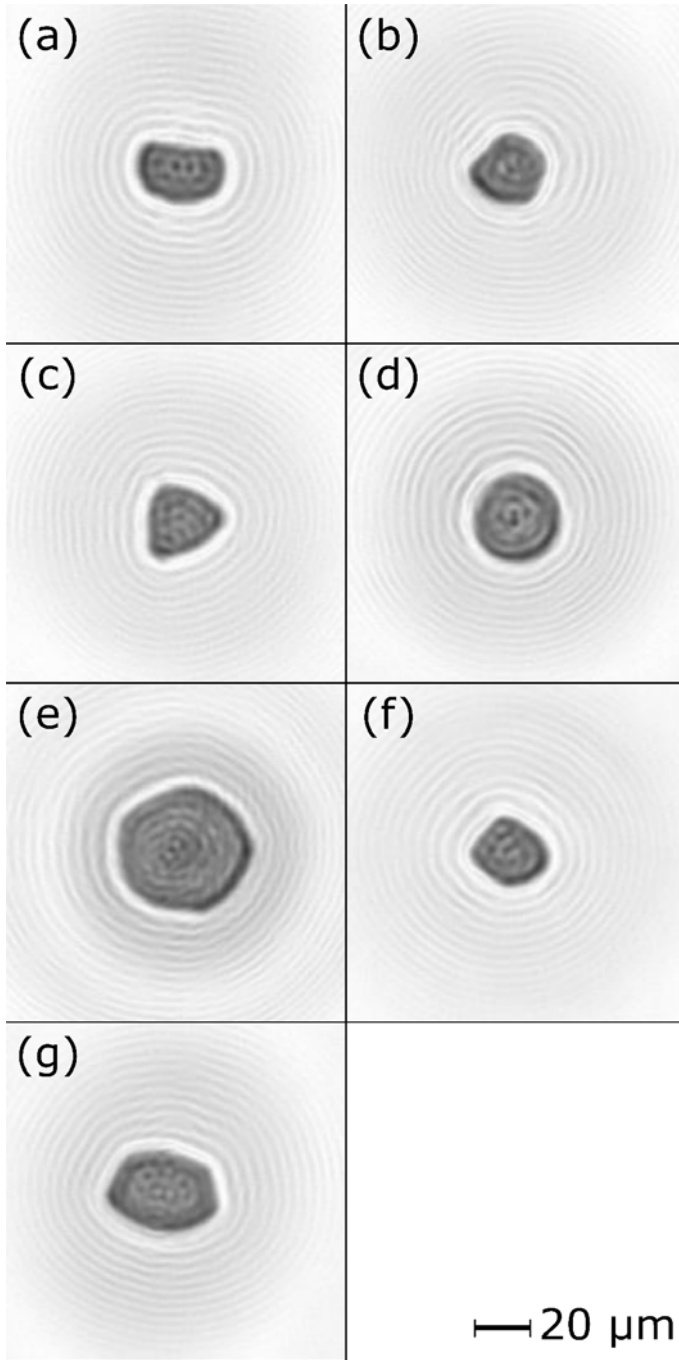
389 Woolcock, Ann J, Shalini A Bastiampillai, Guy B Marks, et Victoria A Keena. (2001). « The Burden of Asthma in Australia ». *Medical Journal of Australia* 175 (3): 141-45. <https://doi.org/10.5694/j.1326-5377.2001.tb143062.x>.

390

391 Woolcock, Ann J., et Jennifer K. Peat. (2007). « Evidence for the Increase in Asthma Worldwide ». In *Ciba Foundation*
392 *Symposium 206 - The Rising Trends in Asthma*, 122-39. John Wiley & Sons, Ltd.
393 <https://doi.org/10.1002/9780470515334.ch8>.

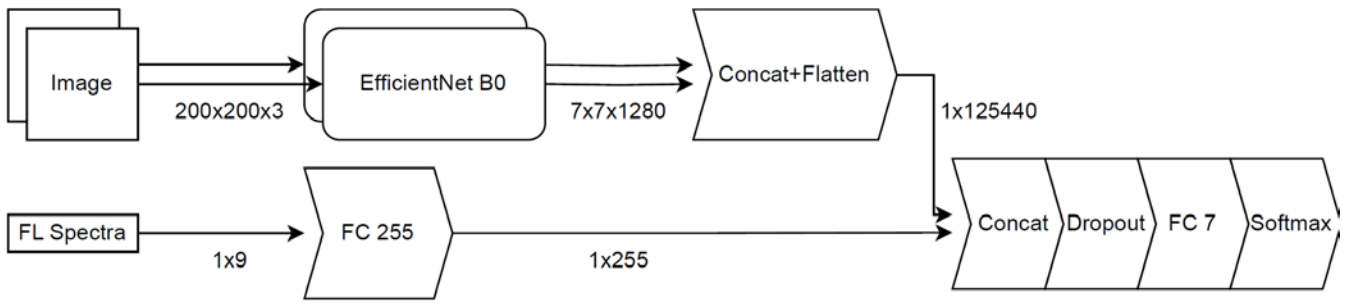
394 Ziello, C., Sparks, T. H., Estrella, N., Belmonte, J., Bergmann, K. C., Bucher, E., ... & Menzel, A. (2012). Changes to airborne
395 pollen counts across Europe. *PloS one*, 7(4), e34076.

396 Zuberbier, Torsten, Jan Lötvall, Steven Simoens, SV Subramanian, et Martin K Church. (2014). « Economic burden of
397 inadequate management of allergic diseases in the European Union: a GA2LEN review ». *Allergy* 69 (10): 1275-79.



399

400 **Figure 1: Holographic images of pollen after numerical reconstruction: (a) *Alnus glutinosa* (b) *Betula pendula*, (c)**
 401 ***Corylus avellana*, (d) *Cynosurus cristatus*, (e) *Fagus sylvatica*, (f) *Fraxinus excelsior*, (g) *Quercus robur***



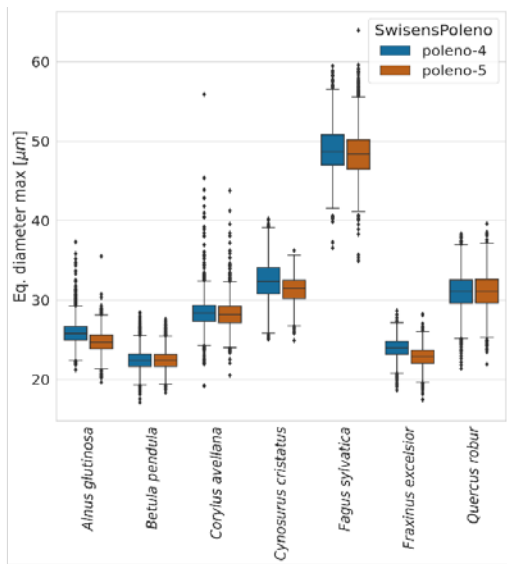
402

403

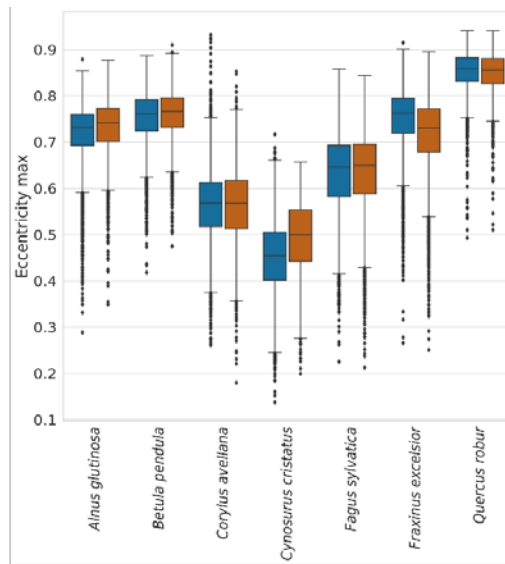
404

405

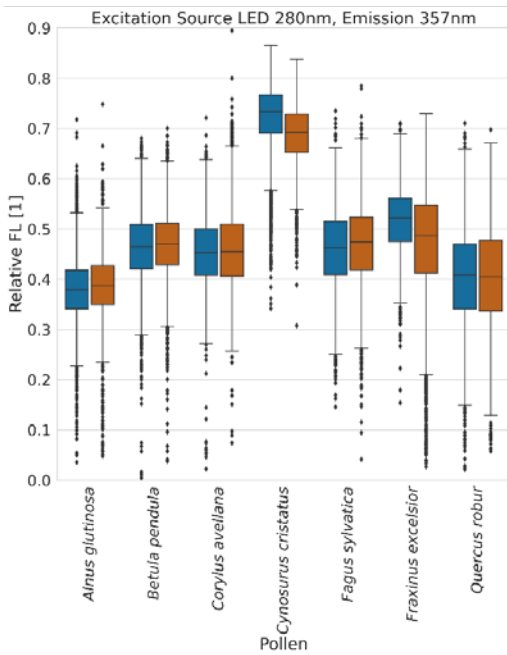
Figure 2: ML model structure used to classify the pollen data. The top path handles the holographic image data while the bottom path processes the relative FL spectra data. The numbers on the connecting lines denote the dimensions of the data.



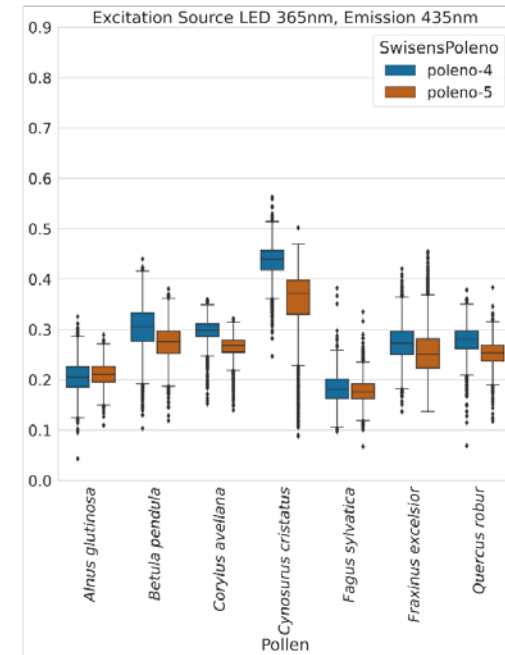
(a)



(b)



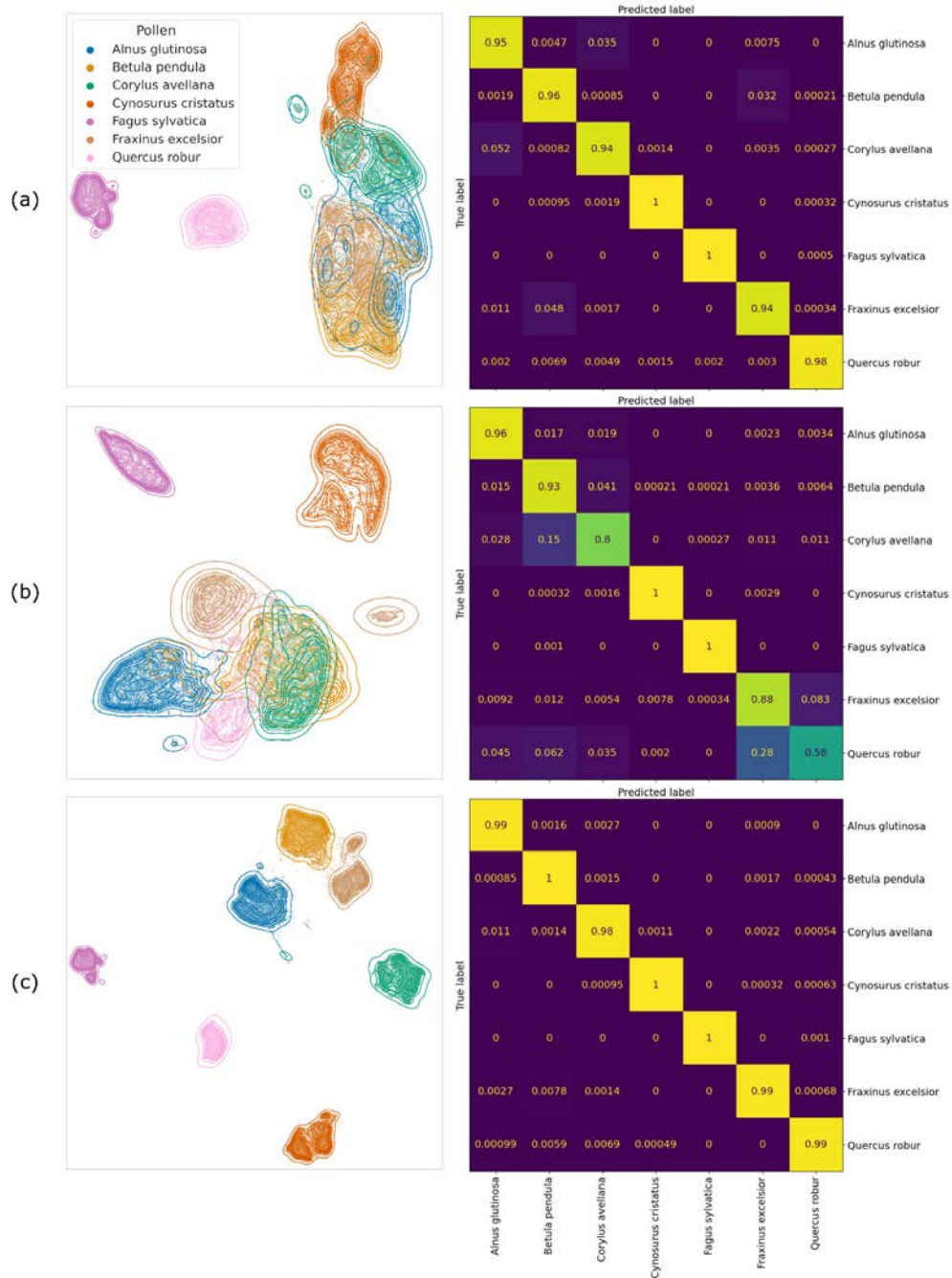
(c)



(d)

406

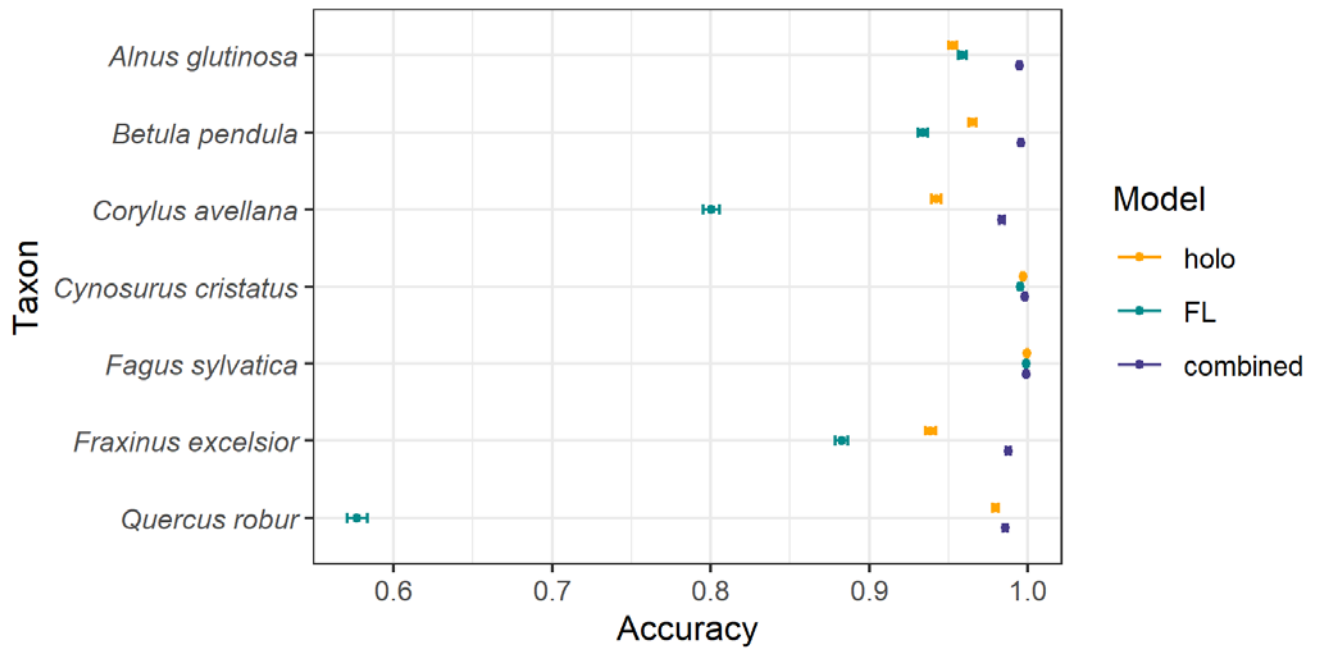
407 **Figure 3: Distribution of holographic image features (upper plots) and relative FL (bottom plots) for each pollen class**
 408 **and measurement system. (a) Maximum equivalent area diameter in μm , defined as the diameter of a circle with the**
 409 **same area as the particle, (b) Maximum eccentricity, defined as the deviation of the ellipse fitted to the particle from a**
 410 **perfect circle, ranging from 0 for a circle to close to 1 for an ellipse. (c) Measured relative FL intensity with 280 nm**
 411 **excitation and detector with centre wavelength 357 nm and (d) with 365 nm excitation and detector 562 nm.**



412

413 **Figure 4: Left side: Uniform Manifold Approximation and Projection (UMAP) of particle features (morphology or/and**
 414 **FL features) of all the data. Right side: Confusion matrices indicating the performance of each model on the test set.**
 415 **Line (a) holography only, line (b) relative FL only and line (c) combined relative FL and holography. UMAP settings:**
 416 **neighbours = 15, minimum distance = 0.001, random state = 42.**

417



418 **Figure 5: Accuracy of each model for each taxon. The error bars represent the 95% confidence intervals.**